Atmos. Chem. Phys., 26, 4423–4437, 2026
https://doi.org/10.5194/acp-26-4423-2026
© Author(s) 2026. This work is distributed under
the Creative Commons Attribution 4.0 License.

Atmospheric Chemistry and Physics
Open Access
EGU

Mechanistic insights into marine boundary layer nucleation: synergistic interactions of typical sulfur, iodine, and nitrogen precursors

Jing Li, An Ning, Ling Liu, Xiucong Deng, and Xiuhui Zhang

State Key Laboratory of Environment Characteristics and Effects for Near-space, Key Laboratory of Cluster Science, Ministry of Education of China, School of Chemistry and Chemical Engineering, Beijing Institute of Technology, Beijing, 100081, China

Correspondence: An Ning (anning@bit.edu.cn) and Xiuhui Zhang (zhangxiuhui@bit.edu.cn)

Received: 13 November 2025 – Discussion started: 20 November 2025
Revised: 10 March 2026 – Accepted: 11 March 2026 – Published: 1 April 2026

Abstract. Marine new particles significantly impact the global atmosphere, yet the key nucleation process underlying their formation remains unclear. Sulfur-, nitrogen-, and iodine-containing species are expected to coexist in the marine atmosphere, including the canonical precursors methanesulfonic acid (MSA), iodic acid (IA), and dimethylamine (DMA). To elucidate how they interact to drive NPF, we performed high-level quantum chemical calculations and cluster dynamics simulations to investigate their synergistic nucleation mechanism at the molecular level. The results show that IA, MSA, and DMA form stable pre-nucleation clusters via intermolecular hydrogen and halogen bonding, with acid-base reactions during clustering, forming ion pairs. The proposed IA–MSA–DMA ternary nucleation is thermodynamically more favorable in regions rich in sulfur and nitrogen but poor in iodine. Its cluster formation rate is notably higher than that of any corresponding binary nucleation, showing a synergistic enhancement of 4–8 orders of magnitude. Moreover, this rate even exceeds that of the well-established efficient iodine oxoacids nucleation under sulfur-rich conditions. In polar coastal regions such as Marambio, the inclusion of the IA–MSA–DMA nucleation pathway brings simulated nucleation rates closer to field measurements than considering the established IA–DMA nucleation alone, identifying it as a critical mechanism in these environments. Accordingly, the proposed IA–MSA–DMA nucleation mechanism is expected to be important in the marine boundary layer, helping to explain the missing sources of marine particles, especially in cold polar marine regions. Incorporating this mechanism into atmospheric modelling can potentially improve aerosol formation simulations and refine climate predictions.

1 Introduction

Marine aerosols represent the largest aerosol system on Earth, influencing global radiative balance and climate change (O'Dowd and Leeuw, 2007; Zhang et al., 2012). Notably, aerosols are the primary source of uncertainty in climate forcing (Gettelman and Kahn, 2025). Aerosols originate primarily from new particle formation (NPF), initiated by nucleation processes that involve the gas-to-particle transition – a critical yet elusive stage (Kulmala et al., 2013). Field studies have shown that marine NPF events are closely linked to iodine-bearing precursors, with iodic acid (HIO_3, IA) playing a key role in driving nucleation (Sipilä et al., 2016; Baccarini et al., 2020; Beck et al., 2021; He et al., 2021; He et al., 2023).

Although IA is abundant and widespread, its self-nucleation is insufficient to explain the fast nucleation observed (Ning et al., 2022a; Ma et al., 2023). Even with the effective stabilization by iodous acid (HIO_2), the predicted nucleation rates cannot fully account for the high values measured in previous experiments (Engsvang and Elm, 2025). As an acidic precursor, IA is readily stabilized by atmospheric base such as ammonia (NH_3) and amines (e.g., dimethylamine, DMA) (Rong et al., 2020; Xia et al., 2020; Ning

et al., 2022b; Ma et al., 2023; Li et al., 2024) via acid-base reactions. Among these bases, DMA stabilizes IA more efficiently – by 1000-fold compared to NH_3 (Ning et al., 2022b). Accordingly, when NH_3 and DMA coexist, IA–DMA clusters play a more important role in nucleation under ambient conditions of boundary layer (Li et al., 2024). A recent study has also confirmed that IA–amine nucleation is efficient enough to be comparable to the well-established sulfuric acid–amine nucleation, provided that IA exceeds sulfuric acid by a factor of 10 (Engsvang and Elm, 2025). However, IA–DMA mechanism overlooks the roles and effects of other effective nucleation precursors, failing to capture the complexity of real atmospheric scenarios.

Alongside the aforementioned efficient iodine (IA) and nitrogen (DMA) precursors, historically, sulfur-containing compounds have also been regarded as vital nucleation agents over oceans, primarily the oxidation product of dimethyl sulfide (DMS) (Hodshire et al., 2019; Hoffmann et al., 2016). As the typical oxidation product of DMS, methanesulfonic acid (MSA) is ubiquitous in marine atmospheres, often present at considerable concentrations (Chen et al., 2018; Dal Maso et al., 2002; Yan et al., 2019; Eisele and Tanner, 1993), and existing observational data may even underestimate its true levels (Yan et al., 2019). More importantly, MSA shows effective nucleation potential, even comparable to that of H_2SO_4 (Liu et al., 2022; Perraud et al., 2015; Dawson et al., 2012), and can individually bind with IA and DMA to form binary clusters, respectively (Ning et al., 2022a; Chen et al., 2016; Chen and Finlayson-Pitts, 2017). Nevertheless, theoretical studies suggest that electrically neutral clusters consisting solely of MSA (as the clustering acid) are unlikely to form and grow under realistic atmospheric conditions (Elm, 2021). Moreover, field observations indicate that MSA frequently coexists with IA and DMA in the marine atmosphere, and all three species are simultaneously detected in aerosol particle (Salignat et al., 2024). Collectively, the evidence points to the coexistence and potential interactions of these typical marine sulfur-(MSA), iodine-(IA), and nitrogen-(DMA) precursors, implying their possibility to jointly participate in particle nucleation. However, whether these three precursors exhibit synergistic effects, as well as the underlying molecular mechanisms and their atmospheric implications, remains unclear. Thus, elucidating the IA–MSA–DMA ternary nucleation process is crucial for a deeper understanding of the underlying origins of marine NPF events.

Herein, we investigated the IA–MSA–DMA ternary nucleation system (denoted as $(IA)_x(MSA)_y(DMA)_z$, where $x+y+z \leq 6$ and $x+y \geq z$) at the molecular level using quantum chemical (QC) calculations and cluster dynamics simulations. QC calculations and wavefunction analyses were performed to clarify the physicochemical nature of clustering, while nucleation rates under varying atmospheric conditions were calculated to reveal nucleation dynamics. By comparing nucleation simulations with field observations (or other well-established nucleation systems), we assess and quantify the importance of IA–MSA–DMA nucleation mechanism. Furthermore, by analyzing the nucleation pathway under different marine conditions, we quantify the contribution of IA–MSA–DMA ternary nucleation to particle formation.

2 Methods

2.1 Quantum Chemistry Calculations

In this study, a multistep conformation search was employed to identify the lowest-energy structures of $(IA)_x(MSA)_y(DMA)_z$ ($1 \leq x+y+z \leq 6, x+y \geq z$) clusters. We considered only clusters in which the number of acid molecules equal to or greater than that of base molecules, as prior computational and experimental studies indicate that clusters with excess base are generally thermodynamically less stable and inefficient for nucleation under atmospherically relevant conditions (Myllys et al., 2019; Ning et al., 2022b). A detailed description of the methodology is provided in the Supplement. The initial structures of pure IA clusters, as well as binary IA–MSA, IA–DMA, and MSA–DMA clusters, were adopted from the previous studies (Rong et al., 2020; Ning et al., 2022a; Ning et al., 2022b; Ning and Zhang, 2022). All lowest-energy structures of IA–MSA–DMA ternary cluster were further optimized using the Gaussian 09 program (Frisch et al., 2009) at the ωB97X-D/6-311++G(3df,3pd) (for C, H, O, N, and S atoms) + aug-cc-pVTZ-PP (for I atom) level of theory (Francl et al., 1982; Peterson et al., 2003). Subsequent single-point energy calculations were carried out using the ORCA 5.0 software (Neese, 2012) at the DLPNO-CCSD(T)/aug-cc-pVTZ (for C, H, O, N, and S atoms) + aug-cc-pVTZ-PP (for I atom) level of theory, with the TightPNO and TightSCF criteria applied to ensure high-accuracy electronic energies. Given the significant impact of spin-orbit coupling (SOC) on energy calculations for heavy elements like iodine (Verstraete et al., 2008; Mohd Zaki et al., 2023; Engsvang et al., 2024), we quantitatively evaluated SOC effects using the Gaussian 16 program (Frisch et al., 2016) at the ωB97X-D/6-311++G(3df,3pd) (for C, H, O, N, and S atoms) + dhf-TZVP-2c (for I atom) level of theory (Chan and Yim, 2013; Kuhn and Weigend, 2015; Sarr et al., 2021; Holzer et al., 2022). Gibbs free energies (ΔG_{ref}, kcal mol^{-1}) of the IA–MSA–DMA clusters under standard pressure were calculated using Eq. (1):

$$\Delta G_{\mathrm{ref}} = \Delta G_{\mathrm{thermal}}^{\omega\mathrm{B97X\text{-}D}} + \Delta E_{\mathrm{DLPNO\text{-}CCSD(T)}} + \Delta E_{\mathrm{SOC}}, \quad (1)$$

where $\Delta G_{\mathrm{thermal}}^{\omega\mathrm{B97X\text{-}D}}$ and $\Delta E_{\mathrm{DLPNO\text{-}CCSD(T)}}$ represent the thermal and electronic contributions to the Gibbs free energy, respectively. ΔE_{SOC} denotes the relativistic correction from SOC for iodine-containing clusters. Thermal corrections ($\Delta G_{\mathrm{thermal}}^{\omega\mathrm{B97X\text{-}D}}$) across the temperature range of 258–298 K were obtained using Shermo 2.0 software (Lu and Chen, 2021). Final Gibbs free energies are summarized in Table S1

of the Supplement. To account for the influence of precursor concentrations, the ΔG_{ref} was further converted to the concentration-dependent Gibbs free energy (ΔG) using Eq. (2):

$$\Delta G(P_1, P_2, \ldots, P_n) = \Delta G_{\mathrm{ref}} - k_{\mathrm{B}} T \sum_{i=1}^{n} N_i \ln\left(\frac{P_i}{P_{\mathrm{ref}}}\right), \quad (2)$$

where P_{ref} is the reference pressure (1 atm), k_{B} is the Boltzman constant, T is the temperature, N_i is the number of molecules i in the cluster, and P_i is the partial pressure of vapor i.

In this study, the conducted ACDC simulations accounted for all feasible collision and evaporation processes. These included interactions between monomer-monomer, monomer-cluster, and cluster-cluster pairs, in addition to the fragmentation of parent clusters into monomers or into two smaller clusters. Furthermore, in our ACDC simulations, the largest clusters considered consist of six molecules (~ 1.2 nm), which fall within the reported atmospheric nucleation critical cluster sizes of 1.1–1.9 nm (Kulmala et al., 2013). The current system size is large enough because the largest cluster included is stable, with its collisions dominating evaporation. This suggests that the cluster size employed here is sufficient for capturing the relevant nucleation behaviour; therefore, the present results are consequently reasonable.

2.2 Wavefunction Analysis

The stability of clusters is largely determined by intermolecular forces between constituent molecules. To gain deeper insight into these interactions within the IA–MSA–DMA clusters, wavefunction-based analyses were performed using the Multiwfn 3.7 program (Lu and Chen, 2012). Specifically, the electrostatic potential (ESP) was projected onto the molecular van der Waals (vdW) surface to identify favorable interaction regions of the nucleating species, namely IA, MSA, and DMA.

2.3 Atmospheric Clusters Dynamic Simulations

The atmospheric cluster dynamic code (ACDC) (McGrath et al., 2012) was utilized to explore the cluster formation rates, growth pathways, and steady-state concentrations of the IA–MSA–DMA system by solving the birth-death equation (see the Supplement for details).

In the ACDC simulation, an enhancement factor of 2.3 was applied to the collision rate coefficient ($\beta_{i,j}$) to account for enhanced intermolecular vdW forces (Halonen et al., 2019), consistent with its validated application in previous nucleation studies (Stolzenburg et al., 2020; Cai et al., 2021; Li et al., 2023; Ning et al., 2024). Additionally, the coagulation sink (S_i) (Lehtipalo et al., 2016), which varies with cluster size, was calculated using Eq. (3):

$$S_i = \mathrm{CS}_{\mathrm{ref}} \times (d_i/d_{\mathrm{ref}})^{-m}, \quad (3)$$

where $\mathrm{CS}_{\mathrm{ref}}$ is the condensation sink (CS) of the reference monomer (i.e., IA monomer), and d denotes the diameter of either the monomer or the cluster. The exponent m, set to 1.7, is dependent on the background aerosol distribution and falls within the typical range reported for atmospheric particles (Lehtinen et al., 2007). A cluster was defined as stable when the product of its collision rate coefficient and concentration ($\beta \cdot C$) surpasses the sum of its evaporation rate constants ($\Sigma\gamma$, Table S2). Such stable clusters were assumed to grow outside the simulated box without evaporating back into the system, and this criterion was applied to set the simulation boundary conditions (detailed in Table S3).

The condition settings for the ACDC simulations were based on data from field measurements, Cosmics Leaving Outdoor Droplets (CLOUD) experiments, and atmospheric modelling. For the marine boundary layer (MBL), the temperature (T) was primarily set within the range of 258–298 K (Almeida et al., 2013), and the CS was set as $2.0 \times 10^{-3}\ \mathrm{s}^{-1}$ (He et al., 2021). The concentration range of precursors was specified as: $[\mathrm{IA}] = 10^6$–10^8 molec. cm^{-3} (Sipilä et al., 2016), $[\mathrm{MSA}] = 10^6$–10^8 molec. cm^{-3} (Berresheim et al., 2002; Chen et al., 2018), and $[\mathrm{DMA}] = 0.025$–2.5 pptv (Yu and Luo, 2014), respectively.

3 Results and Discussion

3.1 Cluster Structure

Strong intermolecular noncovalent interactions are critical in governing the formation and stability of molecular clusters. To assess the synergistic nucleation potential of IA, MSA, and DMA, the surface electrostatic potential (ESP) mapped on van der Waals (vdW) surfaces of these molecules was analyzed using the Multiwfn 3.7 (Lu and Chen, 2012), based on the calculated wavefunctions at the ωB97X-D/6-311++G(3df,3pd) (for C, H, O, N, and S atoms) + aug-cc-pVTZ-PP (for I atom) level of theory. The resulting ESP maps are presented in Fig. 1, where regions of positive and negative potential are depicted in red and blue, respectively. A positive ESP indicates an electrophilic region, suggesting a propensity to function as a donor in hydrogen bond (HB) or halogen bond (XB) interactions. In contrast, a negative ESP denotes a nucleophilic region, which is likely to serve as an acceptor in HB or XB interactions. A more detailed analysis is provided in the Supplement. ESP analysis demonstrates the potential for intermolecular interactions among IA, MSA, and DMA, thereby leading to further clustering.

To structurally elucidate the physicochemical nature of clustering, conformational analysis was performed to reveal the characters of intermolecular interactions within the identified ternary IA–MSA–DMA clusters (Fig. S1), where the red and black dashed lines denote XBs and HBs, respectively. The Cartesian coordinates of the optimized cluster structures are listed in Table S4. Overall. the resulting IA–MSA–DMA clusters are stabilized by a network of HBs and XBs. HBs

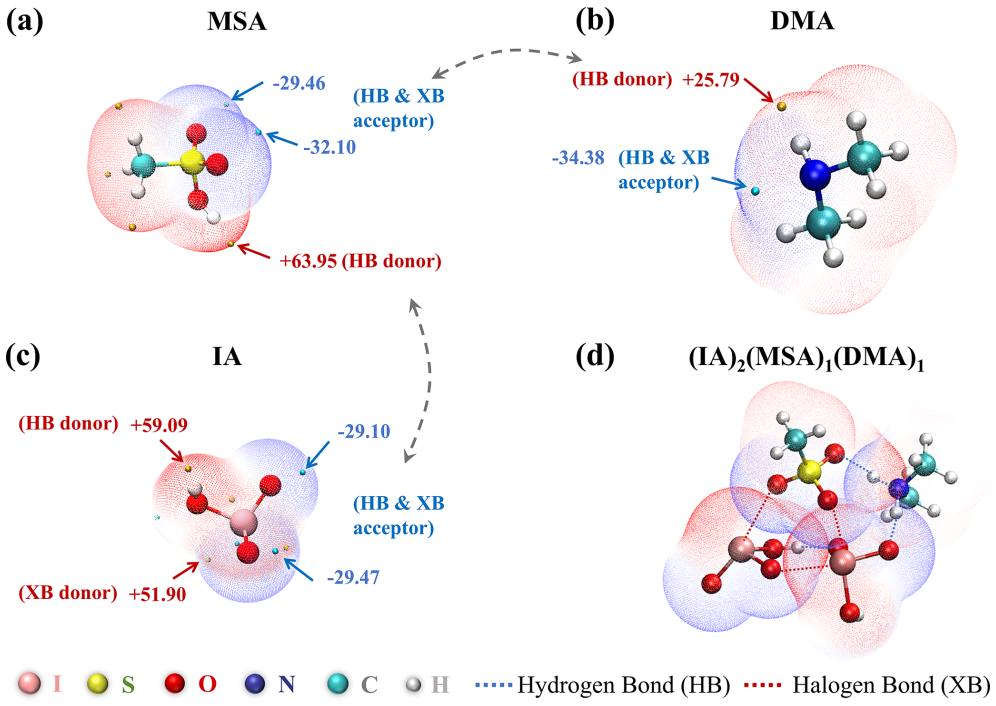

Figure 1. The ESP-mapped molecular vdW surface of **(a)** MSA, **(b)** DMA, **(c)** IA, and **(d)** $(IA)_2(MSA)_1(DMA)_1$ cluster at the ωB97X-D/6-311++G(3df,3pd) (for C, H, O, N, and S atoms) + aug-cc-pVTZ-PP (for I atom) level of theory. The golden and cyan dots represent the positions of maximums and minimums of ESP values (unit: kcal mol^{-1}), respectively. The gray dashed arrows signify the site-to-site interaction tendencies.

are the most prevalent interaction type, constituting ∼ 74 % of all identified non-covalent interactions across all optimized ternary IA–MSA–DMA clusters. Two types of HBs (N–H···O and O–H···O) are observed, with N–H···O HBs dominating (71 %) among the total HB interactions identified and typically forming between acids (IA and MSA) and base (DMA). On the contrary, in the binary IA–DMA system, N–H···O HBs represent a slightly lower proportion (∼ 60 %) and are exclusively formed between IA and DMA. Additionally, both MSA and DMA has methyl groups (–CH_3) that are generally located on the periphery of IA–MSA–DMA clusters. This spatial arrangement facilitates the formation of HBs and XBs, reducing steric hindrance, promoting clustering, and enhancing stability.

During cluster formation, acid-base reactions between acid molecules (IA and MSA) and the base molecule (DMA) often occur, resulting in proton transfer and the formation of ion pairs such as IO_3^-–$DMAH^+$ and $CH_3SO_3^-$–$DMAH^+$. Another distinct feature compared to the binary IA–DMA pathway is the preferential protonation of DMA by the stronger acid MSA (pKa = −1.9 vs. 0.8 for IA), leading to a dominant $CH_3SO_3^-$–$DMAH^+$ ion pair in the ternary system. This provides a different anionic center ($CH_3SO_3^-$) for interaction compared to the IO_3^-–$DMAH^+$ pair within the binary IA–DMA system. This acid-base interaction not only strengthens the cluster via enhanced electrostatic stabilization but also introduces additional interaction sites for noncovalent bonding. As shown in Fig. S2, numerous unoccupied HB and XB sites are present in $(IA)_3(MSA)_1(DMA)_2$ cluster, which can further promote the condensation of atmospheric precursors and the growth of the cluster. These results indicate that IA, MSA, and DMA can form molecular clusters stabilized by a network of HBs and XBs, accompanied by acid-base reactions that produce ion pairs.

3.2 Cluster Stability

To evaluate the thermodynamic stability of the IA–MSA–DMA clusters, concentration-dependent Gibbs free energies (ΔG, Eq. 2) were calculated, and free-energy profiles of the IA–MSA–DMA (ternary) and IA–DMA (binary) pathways were compared under varying precursor concentrations (Fig. 2). Overall, cluster formation energy barriers decrease with increasing precursor concentrations. The key distinction between the IA–MSA–DMA ternary and IA–DMA binary pathway arises in the step where the $(IA)_2(DMA)_1$ cluster grows into either a $(IA)_3(DMA)_1$ or a $(IA)_2(MSA)_1(DMA)_1$ cluster. Thus, our discussion focuses on this critical step.

In Fig. 2a (T = 278 K), as [MSA] increases from 10^6 to 10^8 molec. cm^{-3}, the barrier for the $(IA)_2(DMA)_1$ + IA → $(IA)_3(DMA)_1$ remains constant at 2.54 kcal mol^{-1}, as this step is unaffected by MSA. In contrast, $(IA)_2(DMA)_1$ + MSA → $(IA)_2(MSA)_1(DMA)_1$ requires

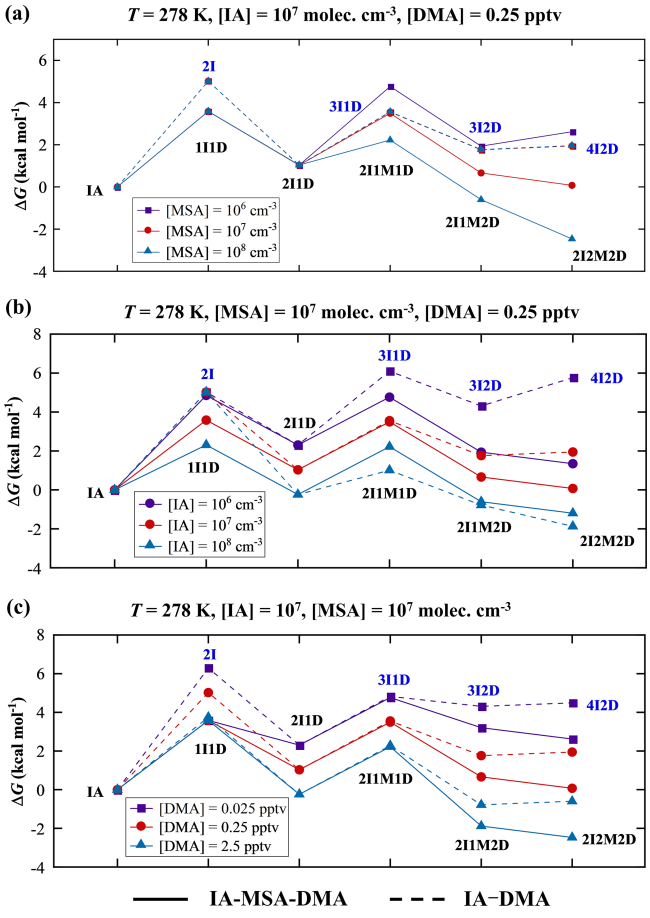

Figure 2. Gibbs free energies of cluster formation (ΔG, kcal mol^{-1}) based on the formation pathway of IA–MSA–DMA ternary (solid lines) and IA–DMA binary (dashed lines) pathways at $T = 278$ K, **(a)** [MSA] = 10^6–10^8 molec. cm^{-3}, **(b)** [IA] = 10^6–10^8 molec. cm^{-3}, **(c)** [DMA] = 0.025–2.5 pptv. I: IA, M: MSA, D: DMA.

3.73 kcal mol^{-1} at [MSA] = 10^6 molec. cm^{-3}, decreases to a level comparable to $(IA)_3(DMA)_1$ formation at [MSA] = 10^7 molec. cm^{-3} (but yields the more stable $(IA)_2(MSA)_2(DMA)_2$ cluster), and further declines to 1.20 kcal mol^{-1} at [MSA] = 10^8 molec. cm^{-3}. These results clearly indicate that higher [MSA] facilitates the IA–MSA–DMA ternary pathway. As shown in Fig. 2b, at [IA] = 10^6 molec. cm^{-3}, formation of $(IA)_2(MSA)_1(DMA)_1$ cluster (2.47 kcal mol^{-1}) is energetically more favorable than $(IA)_3(DMA)_1$ cluster (3.80 kcal mol^{-1}), whereas at [IA] = 10^8 molec. cm^{-3}, the opposite occurs. This suggests that, unlike [MSA], lower [IA] makes the IA–MSA–DMA pathway comparatively less disfavored than the IA–DMA pathway. In Fig. 2c, the energy barriers of the IA–MSA–DMA and IA–DMA pathways are identical at the same [DMA], as the transformation from $(IA)_2(DMA)_1$ cluster to either $(IA)_3(DMA)_1$ or $(IA)_2(MSA)_1(DMA)_1$ cluster proceeds without the involvement of an additional DMA monomer. However, the resulting $(IA)_2(MSA)_2(DMA)_2$ cluster is more stable than $(IA)_4(DMA)_2$, indicating that as [DMA] increases from 0.025 to 2.5 pptv, the IA–MSA–DMA pathway predominates. These results indicate that under the conditions where MSA and DMA are abundant but IA is limited, the IA–DMA pathway becomes thermodynamically unfavorable more rapidly, making the IA–MSA–DMA pathway relatively more favorable.

3.3 Cluster Formation Rate

To assess the potential synergistic enhancement, the cluster formation rate (J, cm^{-3} s^{-1}) of the IA–MSA–DMA system was calculated and compared with the previously reported efficient IA–DMA system (Ning et al., 2022b) using ACDC simulations. As illustrated in Fig. 3a, the simulated J of IA–DMA and IA–MSA–DMA systems exhibit a positive correlation with increasing [IA] under the marine boundary layer (MBL) conditions of $T = 278$ K, CS = 2.0×10^{-3} s^{-1}, [MSA] = 10^6–10^8 molec. cm^{-3}, and [DMA] = 0.25 pptv. In comparison, the IA–MSA–DMA system exhibits significantly higher J values than the IA–DMA system, with similar J observed only at high [IA] ($> 10^7$ molec. cm^{-3}) and low [MSA] (10^6 molec. cm^{-3}), showing a pronounced synergistic enhancement in nucleation. As long as [IA] drops below 10^7 molec. cm^{-3}, IA–MSA–DMA system shows markedly faster nucleation than IA–DMA system, even at the low level of [MSA] (10^6 molec. cm^{-3}). At a moderate [MSA] (10^7 molec. cm^{-3}), the J(IA–MSA–DMA) reaches the order of 10^0–10^2 cm^{-3} s^{-1}, which is up to 10^3 times higher than J(IA–DMA) under the same conditions. Apart from the synergistic effects exhibited by IA–MSA–DMA ternary nucleation, we further compared the nucleation efficiencies of the binary acid–base system: IA–DMA and MSA–DMA systems. Interestingly, although IA exhibits weaker acidity compared to MSA, the resulting J of IA–DMA system significantly exceeds that of the MSA–DMA system by up to approximately four orders of magnitude at same acid levels (Fig. S3). The difference arises from the generally lower ΔGs of IA–DMA clusters relative to MSA–DMA clusters with the same number of molecules, possibly due to the presence of not only HBs but also XBs, which provide additional structural stabilization. It should be noted that this comparison is made under equal acid concentrations to evaluate their nucleation efficiency and does not assume equal atmospheric abundances of IA and MSA. Their atmospheric concentrations are influenced by distinct sources and environmental factors, resulting in temporal and spatial heterogeneity. Taken together, these findings highlight the enhanced nucleation efficiency arising from the synergistic interactions among MSA, IA, and DMA.

To clarify atmospheric relevance of IA–MSA–DMA nucleation in the MBL, the simulated J(IA–MSA–DMA) was compared with that of the well-established IA-iodous acid (HIO_2) system, which has been proposed as a key nu-

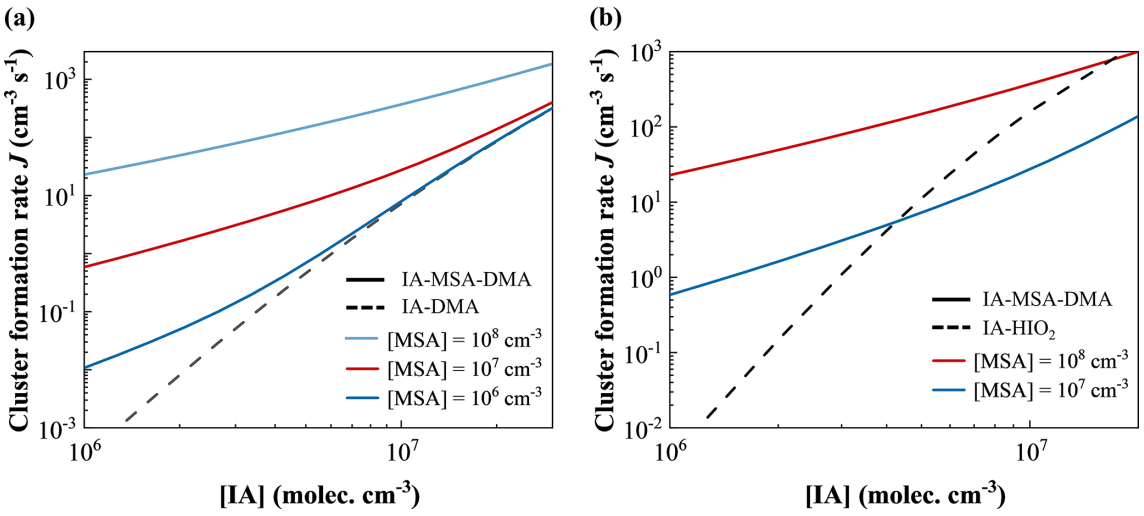

Figure 3. **(a)** Cluster formation rates J ($cm^{-3}\,s^{-1}$) of the IA–DMA and IA–MSA–DMA systems under conditions of $T = 278$ K, CS $= 2.0 \times 10^{-3}\,s^{-1}$, [IA] $= 10^6 - 3.0 \times 10^7$ molec. cm^{-3}, [MSA] $= 10^6$–10^8 molec. cm^{-3}, and [DMA] $= 0.25$ pptv; **(b)** J of the IA–HIO_2 and IA–MSA–DMA systems under conditions of $T = 278$ K, CS $= 2.0 \times 10^{-3}\,s^{-1}$, [IA] $= 10^6 - 2.0 \times 10^7$ molec. cm^{-3}, [MSA] $= 10^7$–10^8 molec. cm^{-3}, and [DMA] $= 0.25$ pptv. [IA]/[HIO_2] is fixed at a value of 50.

cleation mechanism in the MBL (He et al., 2021; Liu et al., 2023; Zhang et al., 2022). As shown in Fig. 3b, at [MSA] $= 10^7$ molec. cm^{-3}, the IA–MSA–DMA system exhibits notably higher J values than the IA–HIO_2 system at lower [IA] ($< 4 \times 10^6$ molec. cm^{-3}), although the latter slightly surpasses the former under higher [IA] conditions. However, when [MSA] increases to 10^8 molec. cm^{-3}, the values of J(IA–MSA–DMA) are almost higher than the J(IA–HIO_2) at the range of [IA] (10^6–10^7 molec. cm^{-3}), with rate enhancements reaching up to four orders of magnitude. This indicates that the proposed IA–MSA–DMA system also represents a highly efficient nucleation mechanism in the MBL. Furthermore, we compared the nucleation rates of the IA–MSA–DMA system with those of the IA–MSA–HIO_2 system. The results indicate that the inclusion of DMA as a strong base in the ternary system markedly enhances cluster formation. Specifically, across the studied temperature and concentration ranges, the calculated nucleation rate for the IA–MSA–DMA mechanism exceeds that of the IA–MSA–HIO_2 system by up to two orders of magnitude (Fig. S4). Collectively, these results highlight the critical role of the synergistic nucleation involving MSA, IA, and DMA, suggesting that IA–MSA–DMA nucleation could represent a key mechanism in the MBL. This mechanism represents a potentially important and previously overlooked NPF nucleation pathway in the MBL.

Furthermore, we compared the nucleation rates of the IA–SA–DMA and IA–MSA–DMA systems at 278 and 248 K (Fig. S5). At 278 K, when the acid concentrations are equal ([SA] = [MSA]), the nucleation rate of the IA–SA–DMA system exceeds that of IA–MSA–DMA by 1–2 orders of magnitude, indicating that sulfuric-acid-driven nucleation is more efficient. This is consistent with sulfuric acid being a stronger nucleating precursor than MSA. However, the relative importance of these pathways in the real atmosphere also depends on the spatiotemporal distribution of their precursor concentrations. Over marine regions, the oxidation of DMS can produce both SO_2 (which is subsequently converted to SA) and MSA. Importantly, the DMS-to-MSA oxidation pathway is temperature dependent, with lower temperatures favoring MSA formation (Chen et al., 2023), potentially leading to enhanced atmospheric MSA accumulation. To reflect this realistic scenario, we compared the systems under colder conditions ($T = 248$ K). Under this temperature, when [SA] = [MSA], the nucleation rate of the IA–MSA–DMA system remains significantly lower than that of the IA–SA–DMA system. However, when the MSA concentration is increased to [MSA] = 5[SA] and [MSA] = 10[SA], the nucleation rate of the IA–MSA–DMA pathway becomes higher. These results confirm that while the SA-driven pathway is effective, the IA–MSA–DMA mechanism we identified is potentially competitive, especially in cold environments where MSA production is enhanced. This underscores that MSA can be a co-dominant driver of iodine-mediated nucleation in specific marine regions.

Additionally, to account for potential uncertainties in quantum chemical calculations and cluster dynamic simulations, we also examined the effects of the calculated ΔG of clusters and the enhancement factor (sticking factor, SF) on J. As shown in Fig. S6, under boundary-layer conditions, variations in the ΔG (± 0.2 kcal mol^{-1}) (Liakos et al., 2020) of clusters and the SF (2.1–2.5) in dynamic simulations lead to only minor changes in J.

3.4 Synergistic Nucleation of IA, MSA, and DMA

As discussed above, the IA–MSA–DMA system shows a synergistic effect on nucleation, resulting in an enhancement on J. To assess this, the included binary acid-base systems, i.e., IA–DMA and MSA–DMA nucleation, were selected as a reference for comparison. Herein, we accordingly define the enhancement factor R as the ratio of J(IA–MSA–DMA) to [J (IA–DMA) + J (MSA–DMA)] (Eq. 4).

$$R = \frac{J(\mathrm{IA}-\mathrm{MSA}-\mathrm{DMA})}{J(\mathrm{IA}-\mathrm{DMA})+J(\mathrm{MSA}-\mathrm{DMA})} = \frac{J([\mathrm{IA}]=x,[\mathrm{MSA}]=y,[\mathrm{DMA}]=z)}{\begin{array}{l}J([\mathrm{IA}]=x,[\mathrm{MSA}]=0,[\mathrm{DMA}]=z)\\ +J([\mathrm{IA}]=0,[\mathrm{MSA}]=y,[\mathrm{DMA}]=z)\end{array}}, \quad (4)$$

where x, y, and z denote the concentrations of IA, MSA, and DMA, respectively.

As shown in Fig. 4a–c, the calculated R increases with rising MSA levels (10^6 to 10^8 molec. cm^{-3}), spanning 1 to 4 orders of magnitude, highlight the efficiency of ternary nucleation. In contrast, with [MSA] and [DMA] held constant, R decreases markedly as [IA] increases. This trend aligns with Fig. 3a, where the gap between J(IA–MSA–DMA) and J(IA–DMA) narrows with rising [IA]. It may be explained by IA's higher efficiency in binding DMA compared to MSA (recalling Sect. 3.3 and Fig. S3), coupled with higher [IA], which amplifies the role of IA–DMA nucleation. It is noteworthy that the contribution of J(MSA–DMA) is negligible, as it is 4–7 orders of magnitude lower than J(IA–DMA). While R is less sensitive to [DMA] compared to [IA], likely due to the relatively narrow range of [DMA] in atmosphere, which constrains its impact. Overall, the R gradually decreases with increasing [IA]. However, at higher [MSA], a slight increase in R is observed, as the presence of MSA counteracts the dominance of the strong IA–DMA binding and enhances the stability of the ternary clusters. These findings suggest that IA–MSA–DMA synergistic nucleation is most relevant in iodine-limited, sulfur-, and nitrogen-rich regions. In addition, the IA–MSA–DMA synergistic nucleation rate shows a sensitivity ranking of IA > DMA > MSA with respect to their concentration variations (Fig. 4d–f). The three-dimensional response surface also shows that when the concentration of any one precursor is held constant, the J increases with the concentration of the other two precursors, indicating significant sensitivity to variations in each component. However, J responds most rapidly to changes in [IA], followed by [DMA], while the response to [MSA] is the slowest (Fig. S7).

3.5 Cluster Formation Pathway

As indicated by the rate analyses, the IA–MSA–DMA synergy enhances nucleation; however, the underlying clustering pathways and their corresponding contribution to particle formation remain unresolved, necessitating further analysis to clarify nucleation dynamics.

As illustrated in Fig. 5a, under the potential MBL conditions of $T = 278$ K, CS $= 2.0 \times 10^{-3}$ s^{-1}, [IA] $= 10^7$ molec. cm^{-3}, [MSA] $= 10^7$ molec. cm^{-3}, and [DMA] $= 0.25$ pptv, the cluster formation pathways of IA–MSA–DMA system can be classified into two types: IA–DMA binary pathway and IA–MSA–DMA ternary pathway. Specifically, IA–DMA clustering pathway proceeds primarily by sequential collisions of IA and DMA monomers, ultimately forming $(IA)_4(DMA)_2$ cluster that is recognized as the boundary cluster (see details in the Supplement), which can grow beyond the simulation system. The dominant nucleation mechanism identified in the ternary IA–MSA–DMA system involves two types of pathways: the ternary IA–MSA–DMA pathway and the binary IA–DMA pathway; notably, at high IA concentrations, the latter effectively reduces to the binary mechanism previously reported by Ning et al. (2022b).

In contrast, the ternary IA–MSA–DMA clustering pathway is more complex. In addition to a stepwise growth route similar to the binary IA–DMA pathway via $(IA)_2(DMA)_1$ cluster, IA monomer can also collide with MSA monomer to form a $(IA)_1(MSA)_1$ heterodimer. The formed $(IA)_1(MSA)_1$ cluster can further collide with DMA monomer to form a $(IA)_1(MSA)_1(DMA)_1$ heterotrimer, which can grow via two routes: (a) colliding with an IA monomer to produce a $(IA)_2(MSA)_1(DMA)_1$ cluster; (b) colliding with a MSA monomer to form a $(IA)_1(MSA)_2(DMA)_1$ cluster. The two clusters can continue to grow, ultimately yielding a $(IA)_2(MSA)_2(DMA)_2$ cluster, which can grow larger to contribute to particle formation. At elevated temperatures of 288–298 K, the IA–MSA–DMA ternary nucleation pathway exhibits notable modifications. As illustrated in Fig. S8, both IA and MSA monomers are capable of alternately colliding with other monomers, ultimately yielding the $(IA)_1(MSA)_2(DMA)_3$ cluster that subsequently undergoes further growth.

To further quantify the relative contributions of different clustering pathways, we performed ACDC simulations to track the molecular-level clustering processes under varying precursor concentrations and temperatures. As shown in Fig. 5b, the contribution of the IA–MSA–DMA pathway (yellow bar) exhibits a pronounced positive dependence on both [MSA] and [DMA]. Specifically, as [MSA] increases from 5.0×10^5 to 5.0×10^7 molec. cm^{-3}, the contribution of IA–MSA–DMA pathway rises sharply from 3 % to 98 %. Similarly, increasing [DMA] from 2.5×10^{-3} to 2.5×10^{-2} pptv results in a substantial enhancement of the pathway contribution from 20 % to 67 %; however, further elevation of [DMA] to 2.5×10^{-1} and 2.5×10^{0} pptv induces only marginal changes, suggesting a base saturation effect. In contrast, the contribution of the IA–MSA–DMA pathway is negatively correlated with [IA]. At [IA] below 10^7 molec. cm^{-3}, the ternary IA–MSA–DMA pathway predominates, whereas at [IA] above this threshold, the binary IA–DMA pathway becomes dominant. Temperature also exerts a significant in-

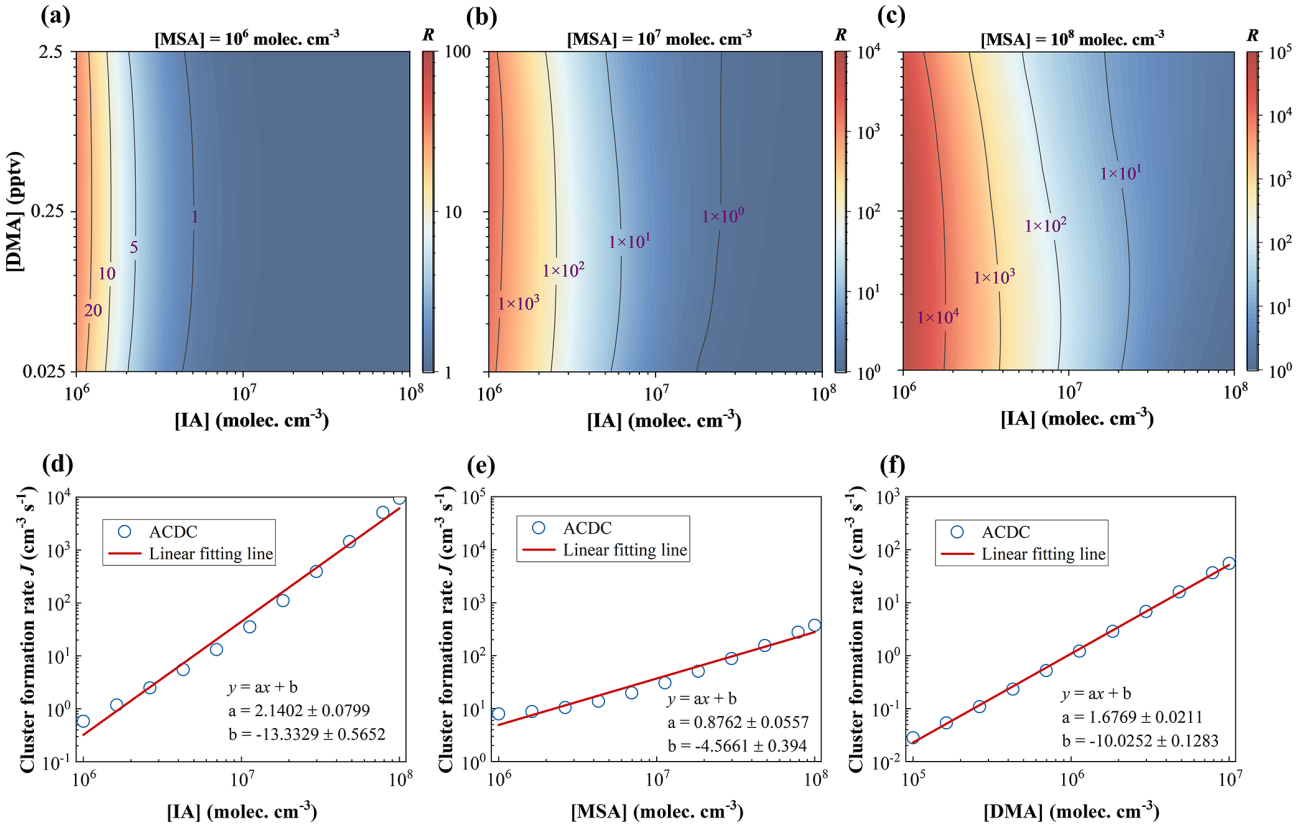

Figure 4. Enhancement factor R for IA–MSA–DMA cluster formation under conditions of $T = 278$ K, CS $= 2.0 \times 10^{-3}$ s^{-1}, [IA] $= 10^6$–10^8 molec. cm^{-3}, [DMA] $= 0.025$–2.5 pptv, and **(a)** [MSA] $= 10^6$, **(b)** 10^7, and **(c)** 10^8 molec. cm^{-3}, respectively. Function dependence of the cluster formation rate (J) on **(d)** [IA] ($r = 0.99$), **(e)** [MSA] ($r = 0.98$), and **(f)** [DMA] ($r = 0.99$), showing a linear relationship.

fluence: as the temperature increases from 258 to 298 K, the relative contribution of the IA–MSA–DMA pathway decreases markedly, with an abrupt decline observed between 278 and 288 K. This may be attributed to a distinct change in the growth pattern of the IA–MSA–DMA pathway when the temperature rises to 288–298 K (Fig. S8). Specifically, the dominant growing cluster shifts from $(IA)_2(MSA)_2(DMA)_2$ at 278 K to $(IA)_1(MSA)_2(DMA)_3$ at 288–298 K, indicating temperature would influence the cluster growth pathway.

Overall, these results demonstrate that the IA–MSA–DMA pathway is highly sensitive to precursor concentrations and temperatures. Its contribution increases strongly with [MSA] and moderately with [DMA] until a saturation effect is reached, while exhibiting a negative dependence on [IA]. Temperature rise significantly suppresses the role of this ternary pathway, especially around 278–288 K. Therefore, this synergistic nucleation involving sulfur (MSA), iodine (IA), and nitrogen (DMA) precursors is most prevalent in cold environments that are rich in sulfur and nitrogen but scarce in iodine, such as polar marine regions. This is consistent with previous studies indicating that the MSA formation is highly temperature-dependent and is enhanced in polar areas (Chen et al., 2023; Scholz et al., 2023), while IA concentrations tend to decrease at high latitudes with lower temperatures, as reflected in the observed decline of iodine monoxide (a key IA precursor) with increasing latitude (Takashima et al., 2022).

3.6 Comparison with Field Observations

To better evaluate the potential atmospheric implications of the proposed IA–MSA–DMA nucleation mechanism, we calculated the cluster formation rate under polar conditions, where the impact of IA–MSA–DMA nucleation is expected to be significant, and further compared the simulations with field observations. As discussed earlier, the IA–MSA–DMA synergistic nucleation is relatively impactful in the cold coastal regions, where [MSA] is relatively higher and [IA] is lower. Accordingly, Marambio was selected for a comparative analysis due to its characteristics: it is located in coastal polar regions, exhibits high [MSA] levels but relatively low [IA], and has a low annual mean temperatures (≤ 273 K) (Quéléver et al., 2022). It should be noted that the field observation data presented here correspond to $J_{1.5}$, whereas our simulated values are $J_{1.2}$. Therefore, to enable a direct comparison, the simulated $J_{1.2}$ values were converted to $J_{1.5}$ according to Eq. (S4).

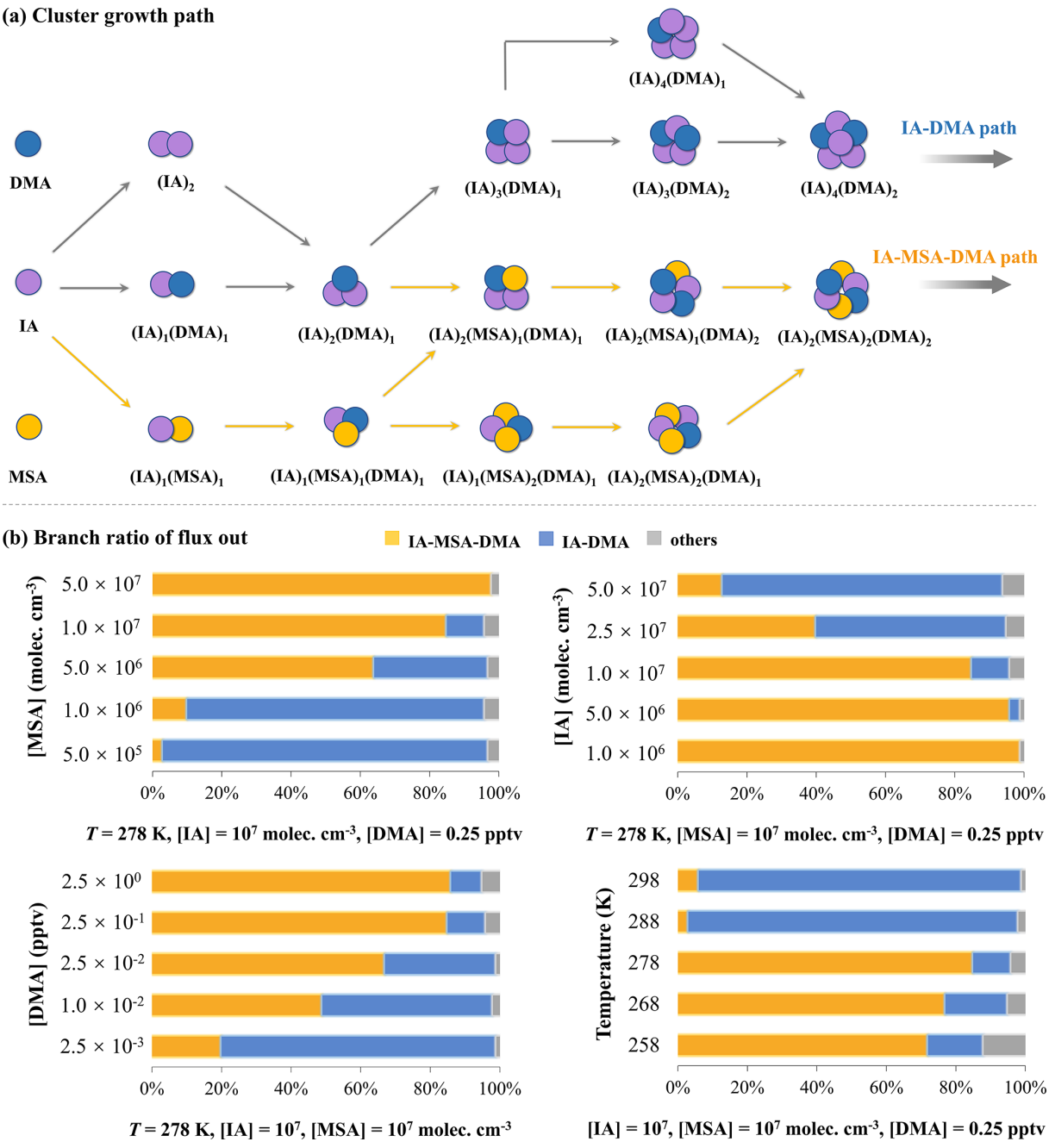

Figure 5. **(a)** The simulated primary cluster growth pathways of IA–MSA–DMA system at the conditions of $T = 278$ K, CS $= 2.0 \times 10^{-3}$ s^{-1}, [IA] $= 10^7$ molec. cm^{-3}, [MSA] $= 10^7$ molec. cm^{-3}, and [DMA] $= 0.25$ pptv; **(b)** Branch ratio of different flux out under the varying [MSA] ($5.0 \times 10^5 - 5.0 \times 10^7$ molec. cm^{-3}), [IA] ($1.0 \times 10^6 - 5.0 \times 10^7$ molec. cm^{-3}), [DMA] ($2.5 \times 10^{-3} - 2.5 \times 10^0$ pptv), and temperatures (258–298 K).

As illustrated in Fig. 6, the J(IA–MSA–DMA) was simulated under the representative atmospheric conditions of $T = 273$ K, CS $= 6.5 \times 10^{-4}$ s^{-1}, [IA] $= 10^4$–10^6 molec. cm^{-3}, [MSA] $= 10^6$–10^7 molec. cm^{-3}, and [DMA] $= 2.0$ pptv (Quéléver et al., 2022; He et al., 2021; Yu and Luo, 2014). The simulated values of J were then compared with field-measured nucleation rates at the coastal Antarctic station Marambio. The results show that, for both the IA–DMA and IA–MSA–DMA systems, the J increases monotonically with [IA]. Notably, the incorporation of MSA markedly enhances the formation rates (orange-shaded region), bringing them into the range of the observed nucleation rate range (0.12–24 cm^{-3} s^{-1}, black dashed lines) (Quéléver et al., 2022). Even at the lower bound of [MSA]

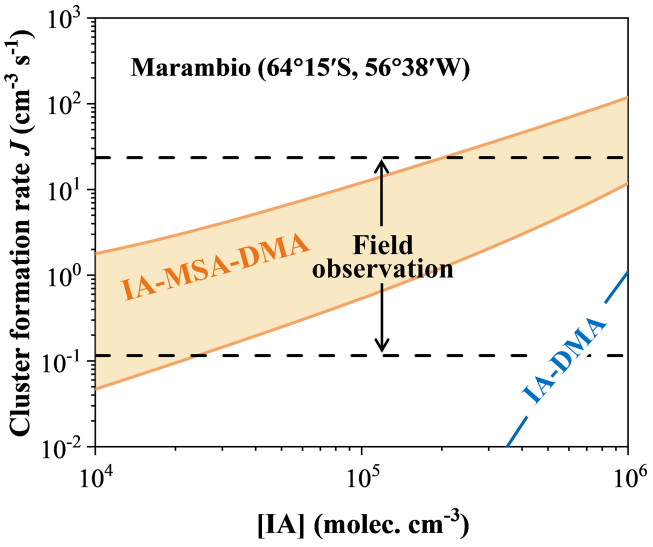

Figure 6. Comparison with the simulated cluster formation rate (J, $cm^{-3}\,s^{-1}$) and field observations under the ambient conditions of Marambio ($T = 273\,K$, $CS = 6.5 \times 10^{-4}\,s^{-1}$, $[IA] = 10^4$–10^6 molec. cm^{-3}, $[MSA] = 10^6$–10^7 molec. cm^{-3}, and $[DMA] = 2.0$ pptv). The orange area, blue line, and black line represent J(IA–MSA–DMA), J(IA–DMA), and J(field observation), respectively. The shaded area corresponds to the nucleation rates simulated at $[MSA] = 10^6$–10^7 molec. cm^{-3}. The dashed field-observation ranges for J at Marambio (0.1–24 $cm^{-3}\,s^{-1}$) is based on the reported $J_{1.5}$ values from Quéléver et al. (2022).

(10^6 molec. cm^{-3}, lower orange solid line), the simulated formation rates are comparable to, though generally higher than, the minimum observed value (0.12 $cm^{-3}\,s^{-1}$, lower black dashed line). Moreover, at lower IA levels, the effect of MSA is pronounced, and ternary nucleation driven by synergistic effects can produce formation rates comparable to those observed. Conversely, under high IA conditions (exceeding approximately 6×10^5 molec. cm^{-3}), the contribution of the IA–DMA pathway becomes increasingly prominent and can account for a portion of the nucleation rate. Overall, the MSA-enhanced ternary nucleation yields rates that fall within the range observed at Marambio across the measured range of [IA], particularly under low-MSA conditions. Even at the highest IA levels, this reproduction cannot be fully captured by the IA–DMA binary mechanism alone.

It should be noted that the nucleation rates presented here, particularly at the upper end of the concentration ranges considered, represent the theoretical results under ideal conditions of concurrently high precursor levels. In the marine atmosphere, temporal and spatial variations in the concentrations of IA, MSA, and DMA will modulate the rates. Moreover, our simulations only consider a limited subset of the atmospheric system, namely clusters containing IA, MSA, and DMA. In reality, additional species and processes may also affect particle formation. For example, Quéléver et al. (2022) showed that sulfuric acid is also observed during NPF events at Marambio, and ammonia can also participate in nucleation processes. In addition, ions and water vapor, which are not included in our model, may further influence cluster stability and formation. If all these factors were incorporated, the predicted formation rates would increase even further. Therefore, the simulated rates should be interpreted as the contribution from a specific IA-MSA-DMA nucleation pathway, rather than a complete description of Antarctic coastal NPF events. Future work should further consider the combined influence of other precursors. Nevertheless, our proposed synergistic mechanism of the ternary IA–MSA–DMA nucleation provides a critical mechanistic understanding for periods and regions where these precursors co-exist at significant levels.

4 Conclusions

Marine aerosol significantly influences the Earth's radiative balance and climate system, yet the fundamental nucleation mechanism in aerosol formation is highly unclear. Despite the recognition of sulfur-, iodine-, and nitrogen-containing chemicals as vital nucleating precursors, whether they can interact and synergistically contribute to nucleation remains unknown.

To address this gap, we systematically investigated the ternary nucleation system involving methanesulfonic acid (MSA, sulfur-containing), iodic acid (IA, iodine-containing), and dimethylamine (DMA, nitrogen-containing) via high-level quantum chemical calculations and atmospheric cluster dynamics simulations. The main findings of this study are as follows: (1) the stable prenucleation cluster composed of IA, MSA, and DMA is mainly stabilized by intermolecular hydrogen bonds (74 %), together with contributions from halogen bonding (XB) and electrostatic attractions between ion pairs produced via acid-base reactions (i.e., $CH_3SO_3^-$–$DMAH^+$ and IO_3^-–$DMAH^+$). (2) The nucleation dynamics of the IA–MSA–DMA system exhibits a pronounced synergistic effect, leading to an enhancement in nucleation rates by 4–8 orders of magnitude compared with the included binary IA–DMA or MSA–DMA systems; under sulfur-rich conditions, the resulting rate even surpasses that of the efficient IA–iodous acid (HIO_2) nucleation mechanism. (3) Mechanistic analysis indicates that the IA–MSA–DMA ternary nucleation can be evident under cold, sulfur- and nitrogen-rich conditions, and the simulated rates under polar-site conditions (Marambio) are comparable to the range of field observations, providing insights into the potential role of this mechanism in observed NPF events.

Although this work highlights the nucleation potential of the IA–MSA–DMA pathway, it does not imply that this mechanism dominates marine nucleation. Rather, our intention is to illustrate the potential synergy among representative marine iodine-, sulfur-, and nitrogen-containing precur-

sors using IA, MSA, and DMA as a tractable model system. In reality, marine nucleation precursors extend far beyond this simplified combination. Sulfuric acid (SA) is widely recognized as a stronger nucleating sulfur-containing precursor than MSA, while iodine oxoacids such as HIO_2 can effectively stabilize HIO_3-containing clusters. Other nitrogen-containing bases, including methylamine, trimethylamine, and NH_3, may also contribute to enhancing nucleation, with their importance largely determined by their spatiotemporal distributions in marine environments. Although explicitly accounting for all these interacting species remains challenging, it is reasonable to expect that when they coexist, additional precursors such as SA and HIO_2 may substantially influence nucleation. In this context, MSA may act as a complementary nucleating acid that enhances SA-driven nucleation, as suggested in previous studies (e.g., Bork et al., 2014). Therefore, the IA–MSA–DMA pathway proposed here likely represents only minor part of a broader multicomponent nucleation network in marine atmospheres, but identifying this MSA-assisted pathway helps reveal how iodine-, sulfur-, and nitrogen-containing precursors may jointly contribute to marine particle formation.

In a word, the findings of this study advance our understanding of marine nucleation by highlighting the synergistic role of sulfur, iodine, and nitrogen precursors – an effect that was previously ignored in binary nucleation frameworks. Incorporating the IA–MSA–DMA mechanism into atmospheric models holds potential to refine parameterizations of marine aerosol formation, reducing uncertainties in climate forcing predictions.

Data availability. The data that supports the findings of this study is openly available in the Zenodo repository at https://doi.org/10.5281/zenodo.18984315 (Li et al., 2026).

Supplement. The supplement related to this article is available online at https://doi.org/10.5194/acp-26-4423-2026-supplement.

Author contributions. XZ designed and supervised the research. JL, XD, and AN performed the quantum chemical calculations and the ACDC simulations. JL, AN, and LL analyzed data. JL, AN, and XZ wrote the paper with contributions from all the other co-authors.

Competing interests. The contact author has declared that none of the authors has any competing interests.

Disclaimer. Publisher's note: Copernicus Publications remains neutral with regard to jurisdictional claims made in the text, published maps, institutional affiliations, or any other geographical representation in this paper. The authors bear the ultimate responsibility for providing appropriate place names. Views expressed in the text are those of the authors and do not necessarily reflect the views of the publisher.

Acknowledgements. This work is funded by the National Science Fund for Distinguished Young Scholars (grant no. 22225607), the National Natural Science Foundation of China (grant nos. 22306011 and 22376013), and the China Postdoctoral Science Foundation (grant no. 2025M784255). Furthermore, we thank for the technical support of the National Large Scientific and Technological Infrastructure "Earth System Numerical Simulation Facility" (https://cstr.cn/31134.02.EL, last access: 5 February 2026).

Financial support. This research has been supported by the National Science Fund for Distinguished Young Scholars (grant no. 22225607), the National Natural Science Foundation of China (grant nos. 22306011 and 22376013), and the China Postdoctoral Science Foundation (grant no. 2025M784255).

Review statement. This paper was edited by Bingbing Wang and reviewed by Morten Engsvang, Jonas Elm, and two anonymous referees.

References

Almeida, J., Schobesberger, S., Kürten, A., Ortega, I. K., Kupiainen-Määttä, O., Praplan, A. P., Adamov, A., Amorim, A., Bianchi, F., Breitenlechner, M., David, A., Dommen, J., Donahue, N. M., Downard, A., Dunne, E., Duplissy, J., Ehrhart, S., Flagan, R. C., Franchin, A., Guida, R., Hakala, J., Hansel, A., Heinritzi, M., Henschel, H., Jokinen, T., Junninen, H., Kajos, M., Kangasluoma, J., Keskinen, H., Kupc, A., Kurten, T., Kvashin, A. N., Laaksonen, A., Lehtipalo, K., Leiminger, M., Leppä, J., Loukonen, V., Makhmutov, V., Mathot, S., McGrath, M. J., Nieminen, T., Olenius, T., Onnela, A., Petäjä, T., Riccobono, F., Riipinen, I., Rissanen, M., Rondo, L., Ruuskanen, T., Santos, F. D., Sarnela, N., Schallhart, S., Schnitzhofer, R., Seinfeld, J. H., Simon, M., Sipilä, M., Stozhkov, Y., Stratmann, F., Tomé, A., Tröstl, J., Tsagkogeorgas, G., Vaattovaara, P., Viisanen, Y., Virtanen, A., Vrtala, A., Wagner, P. E., Weingartner, E., Wex, H., Williamson, C., Wimmer, D., Ye, P., Yli-Juuti, T., Carslaw, K. S., Kulmala, M., Curtius, J., Baltensperger, U., Worsnop, D. R., Vehkamäki, H., and Kirkby, J.: Molecular understanding of sulphuric acid–amine particle nucleation in the atmosphere, Nature, 502, 359–363, https://doi.org/10.1038/nature12663, 2013.

Baccarini, A., Karlsson, L., Dommen, J., Duplessis, P., Vullers, J., Brooks, I. M., Saiz-Lopez, A., Salter, M., Tjernstrom, M., Baltensperger, U., Zieger, P., and Schmale, J.: Frequent new particle formation over the high Arctic pack ice by enhanced iodine emissions, Nat. Commun., 11, 4924, https://doi.org/10.1038/s41467-020-18551-0, 2020.

Beck, L. J., Sarnela, N., Junninen, H., Hoppe, C. J. M., Garmash, O., Bianchi, F., Riva, M., Rose, C., Peräkylä, O., Wimmer, D., Kausiala, O., Jokinen, T., Ahonen, L., Mikkilä, J., Hakala, J., He, X. C., Kontkanen, J., Wolf, K. K. E., Cappelletti, D., Mazzola, M., Traversi, R., Petroselli, C., Viola, A. P., Vitale, V.,

Lange, R., Massling, A., Nøjgaard, J. K., Krejci, R., Karlsson, L., Zieger, P., Jang, S., Lee, K., Vakkari, V., Lampilahti, J., Thakur, R. C., Leino, K., Kangasluoma, J., Duplissy, E. M., Siivola, E., Marbouti, M., Tham, Y. J., Saiz-Lopez, A., Petäjä, T., Ehn, M., Worsnop, D. R., Skov, H., Kulmala, M., Kerminen, V. M., and Sipilä, M.: Differing Mechanisms of New Particle Formation at Two Arctic Sites, Geophys. Res. Lett., 48, e2020GL091334, https://doi.org/10.1029/2020gl091334, 2021.

Berresheim, H., Elste, T., Rosman, K., Dal Maso, M., Tremmel, H. G., Mäkelä, J. M., Allen, A. G., Kulmala, M., and Hansson, H.-C.: Gas-aerosol relationships of H_2SO_4, MSA, and OH: Observations in the coastal marine boundary layer at Mace Head, Ireland, J. Geophys. Res.-Atmos., 107, PAR 5-1–PAR 5-12, https://doi.org/10.1029/2000jd000229, 2002.

Bork, N., Elm, J., Olenius, T., and Vehkamäki, H.: Methane sulfonic acid-enhanced formation of molecular clusters of sulfuric acid and dimethyl amine, Atmos. Chem. Phys., 14, 12023–12030, https://doi.org/10.5194/acp-14-12023-2014, 2014.

Cai, R., Yan, C., Yang, D., Yin, R., Lu, Y., Deng, C., Fu, Y., Ruan, J., Li, X., Kontkanen, J., Zhang, Q., Kangasluoma, J., Ma, Y., Hao, J., Worsnop, D. R., Bianchi, F., Paasonen, P., Kerminen, V.-M., Liu, Y., Wang, L., Zheng, J., Kulmala, M., and Jiang, J.: Sulfuric acid–amine nucleation in urban Beijing, Atmos. Chem. Phys., 21, 2457–2468, https://doi.org/10.5194/acp-21-2457-2021, 2021.

Chan, B. and Yim, W. L.: Accurate Computation of Cohesive Energies for Small to Medium-Sized Gold Clusters, J. Chem. Theory Comput., 9, 1964–1970, https://doi.org/10.1021/ct400047y, 2013.

Chen, H. and Finlayson-Pitts, B. J.: New Particle Formation from Methanesulfonic Acid and Amines/Ammonia as a Function of Temperature, Environ. Sci. Technol., 51, 243–252, https://doi.org/10.1021/acs.est.6b04173, 2017.

Chen, H., Varner, M. E., Gerber, R. B., and Finlayson-Pitts, B. J.: Reactions of Methanesulfonic Acid with Amines and Ammonia as a Source of New Particles in Air, J. Phys. Chem. B., 120, 1526–1536, https://doi.org/10.1021/acs.jpcb.5b07433, 2016.

Chen, J., Lane, J. R., Bates, K. H., and Kjaergaard, H. G.: Atmospheric Gas-Phase Formation of Methanesulfonic Acid, Environ. Sci. Technol., 57, 21168–21177, https://doi.org/10.1021/acs.est.3c07120, 2023.

Chen, Q., Sherwen, T., Evans, M., and Alexander, B.: DMS oxidation and sulfur aerosol formation in the marine troposphere: a focus on reactive halogen and multiphase chemistry, Atmos. Chem. Phys., 18, 13617–13637, https://doi.org/10.5194/acp-18-13617-2018, 2018.

Dal Maso, M., Kulmala, M., Lehtinen, K. E. J., Mäkelä, J. M., Aalto, P., and O'Dowd, C. D.: Condensation and coagulation sinks and formation of nucleation mode particles in coastal and boreal forest boundary layers, J. Geophys. Res.-Atmos., 107, PAR 2-1–PAR 2-10, https://doi.org/10.1029/2001jd001053, 2002.

Dawson, M. L., Varner, M. E., Perraud, V., Ezell, M. J., Gerber, R. B., and Finlayson-Pitts, B. J.: Simplified mechanism for new particle formation from methanesulfonic acid, amines, and water via experiments and ab initio calculations, P. Natl. Acad. Sci. USA, 109, 18719–18724, https://doi.org/10.1073/pnas.1211878109, 2012.

Eisele, F. L. and Tanner, D. J.: Measurement of the gas phase concentration of H_2SO_4 and methane sulfonic acid and estimates of H_2SO_4 production and loss in the atmosphere, J. Geophys. Res., 98, 9001–9010, https://doi.org/10.1029/93JD00031, 1993.

Elm, J.: Clusteromics II: Methanesulfonic acid–base cluster formation, ACS Omega, 6, 17035–17044, https://doi.org/10.1021/acsomega.1c02115, 2021.

Engsvang, M. and Elm, J.: Iodine Clusters in the Atmosphere II: Cluster Formation Potential of Iodine Oxyacids and Iodine Oxides, ACS Omega, 10, 24887–24896, https://doi.org/10.1021/acsomega.5c02147, 2025.

Engsvang, M., Wu, H., and Elm, J.: Iodine clusters in the atmosphere I: Computational benchmark and dimer formation of oxyacids and oxides, ACS Omega, 9, 31521–31532, https://doi.org/10.1021/acsomega.4c01235, 2024.

Francl, M. M., Pietro, W. J., Hehre, W. J., Binkley, J. S., Gordon, M. S., DeFrees, D. J., and Pople, J. A.: Self-consistent molecular orbital methods. XXIII. A polarization-type basis set for second-row elements, J. Chem. Phys., 77, 3654–3665, https://doi.org/10.1063/1.444267, 1982.

Frisch, M. J., Trucks, G. W., Schlegel, H. B., Scuseria, G. E., Robb, M. A., Cheeseman, J. R., Scalmani, G., Barone, V., Mennucci, B., Petersson, G. A., Nakatsuji, H., Caricato, M., Li, X., Hratchian, H. P., Izmaylov, A. F., Bloino, J., Zheng, G., Sonnenberg, J. L., Hada, M., Ehara, M., Toyota, K., Fukuda, R., Hasegawa, J., Ishida, M., Nakajima, T., Honda, Y., Kitao, O., Nakai, H., Vreven, T., Montgomery, J. A., Peralta, J. E., Ogliaro, F., Bearpark, M., Heyd, J. J., Brothers, E., Kudin, K. N., Staroverov, V. N., Kobayashi, R., Normand, J., Raghavachari, K., Rendell, A., Burant, J. C., Iyengar, S. S., Tomasi, J., Cossi, M., Rega, N., Millam, J. M., Klene, M., Knox, J. E., Cross, J. B., Bakken, V., Adamo, C., Jaramillo, J., Gomperts, R., Stratmann, R. E., Yazyev, O., Austin, A. J., Cammi, R., Pomelli, C., Ochterski, J. W., Martin, R. L., Morokuma, K., Zakrzewski, V. G., Voth, G. A., Salvador, P., Dannenberg, J. J., Dapprich, S., Daniels, A. D., Farkas, O., Foresman, J. B., Ortiz, J. V., Cioslowski, J., and Fox, D. J.: Gaussian 09, Revision A.02, Gaussian Inc, Wallingford CT, http://gaussian.com/g09citation/ (last access: 7 May 2022), 2009.

Frisch, M. J., Trucks, G. W., Schlegel, H. B., Scuseria, G. E., Robb, M. A., Cheeseman, J. R., Scalmani, G., Barone, V., Mennucci, B., Petersson, G. A., Nakatsuji, H., Caricato, M., Li, X., Hratchian, H. P., Izmaylov, A. F., Bloino, J., Zheng, G., Sonnenberg, J. L., Hada, M., Ehara, M., Toyota, K., Fukuda, R., Hasegawa, J., Ishida, M., Nakajima, T., Honda, Y., Kitao, O., Nakai, H., Vreven, T., Montgomery, J. A., Peralta, J. E., Ogliaro, F., Bearpark, M., Heyd, J. J., Brothers, E., Kudin, K. N., Staroverov, V. N., Kobayashi, R., Normand, J., Raghavachari, K., Rendell, A., Burant, J. C., Iyengar, S. S., Tomasi, J., Cossi, M., Rega, N., Millam, J. M., Klene, M., Knox, J. E., Cross, J. B., Bakken, V., Adamo, C., Jaramillo, J., Gomperts, R., Stratmann, R. E., Yazyev, O., Austin, A. J., Cammi, R., Pomelli, C., Ochterski, J. W., Martin, R. L., Morokuma, K., Zakrzewski, V. G., Voth, G. A., Salvador, P., Dannenberg, J. J., Dapprich, S., Daniels, A. D., Farkas, O., Foresman, J. B., Ortiz, J. V., Cioslowski, J., and Fox, D. J.: Gaussian 16, Revision A.03, Gaussian Inc, Wallingford CT, https://gaussian.com/gaussian16/ (last access: 20 November 2023), 2016.

Gettelman, A. and Kahn, R.: Aerosols are critical for "nowcasting" climate, One Earth, 8, 101239, https://doi.org/10.1016/j.oneear.2025.101239, 2025.

Halonen, R., Zapadinsky, E., Kurtén, T., Vehkamäki, H., and Reischl, B.: Rate enhancement in collisions of sulfuric acid molecules due to long-range intermolecular forces, Atmos. Chem. Phys., 19, 13355–13366, https://doi.org/10.5194/acp-19-13355-2019, 2019.

He, X.-C., Tham, Y. J., Dada, L., Wang, M., Finkenzeller, H., Stolzenburg, D., Iyer, S., Simon, M., Kürten, A., Shen, J., Roerup, B., Rissanen, M., Schobesberger, S., Baalbaki, R., Wang, D. S., Koenig, T. K., Jokinen, T., Sarnela, N., Beck, L. J., Almeida, J., Amanatidis, S., Amorim, A., Ataei, F., Baccarini, A., Bertozzi, B., Bianchi, F., Brilke, S., Caudillo, L., Chen, D., Chiu, R., Chu, B., Dias, A., Ding, A., Dommen, J., Duplissy, J., Haddad, I. E., Carracedo, L. G., Granzin, M., Hansel, A., Heinritzi, M., Hofbauer, V., Junninen, H., Kangasluoma, J., Kemppainen, D., Kim, C., Kong, W., Krechmer, J. E., Kvashin, A., Laitinen, T., Lamkaddam, H., Lee, C. P., Lehtipalo, K., Leiminger, M., Li, Z., Makhmutov, V., Manninen, H. E., Marie, G., Marten, R., Mathot, S., Mauldin, R. L., Mentler, B., Moehler, O., Mueller, T., Nie, W., Onnela, A., Petaja, T., Pfeifer, J., Philippov, M., Ranjithkumar, A., Saiz-Lopez, A., Salma, I., Scholz, W., Schuchmann, S., Schulze, B., Steiner, G., Stozhkov, Y., Tauber, C., Tome, A., Thakur, R. C., Vaisanen, O., Vazquez-Pufleau, M., Wagner, A. C., Wang, Y., Weber, S. K., Winkler, P. M., Wu, Y., Xiao, M., Yan, C., Ye, Q., Ylisirnio, A., Zauner-Wieczorek, M., Zha, Q., Zhou, P., Flagan, R. C., Curtius, J., Baltensperger, U., Kulmala, M., Kerminen, V.-M., Kurten, T., Donahue, N. M., Volkamer, R., Kirkby, J., Worsnop, D. R., and Sipila, M.: Role of iodine oxoacids in atmospheric aerosol nucleation, Science, 371, 589–595, https://doi.org/10.1126/science.abe0298, 2021.

He, X.-C., Simon, M., Iyer, S., Xie, H.-B., Rörup, B., Shen, J., Finkenzeller, H., Stolzenburg, D., Zhang, R., Baccarini, A., Tham, Y. J., Wang, M., Amanatidis, S., Piedehierro, A. A., Amorim, A., Baalbaki, R., Brasseur, Z., Caudillo, L., Chu, B., Dada, L., Duplissy, J., Haddad, I. E., Flagan, R. C., Granzin, M., Hansel, A., Heinritzi, M., Hofbauer, V., Jokinen, T., Kemppainen, D., Kong, W., Krechmer, J., Kürten, A., Lamkaddam, H., Lopez, B., Ma, F., Mahfouz, N. G. A., Makhmutov, V., Manninen, H. E., Marie, G., Marten, R., Massabò, D., Mauldin, R. L., Mentler, B., Onnela, A., Petäjä, T., Pfeifer, J., Philippov, M., Ranjithkumar, A., Rissanen, M. P., Schobesberger, S., Scholz, W., Schulze, B., Surdu, M., Thakur, R. C., Tomé, A., Wagner, A. C., Wang, D., Wang, Y., Weber, S. K., Welti, A., Winkler, P. M., Zauner-Wieczorek, M., Baltensperger, U., Curtius, J., Kurtén, T., Worsnop, D. R., Volkamer, R., Lehtipalo, K., Kirkby, J., Donahue, N. M., Sipilä, M., and Kulmala, M.: Iodine oxoacids enhance nucleation of sulfuric acid particles in the atmosphere, Science, 382, 1308–1314, https://doi.org/10.1126/science.adh2526, 2023.

Hodshire, A. L., Campuzano-Jost, P., Kodros, J. K., Croft, B., Nault, B. A., Schroder, J. C., Jimenez, J. L., and Pierce, J. R.: The potential role of methanesulfonic acid (MSA) in aerosol formation and growth and the associated radiative forcings, Atmos. Chem. Phys., 19, 3137–3160, https://doi.org/10.5194/acp-19-3137-2019, 2019.

Hoffmann, E. H., Tilgner, A., Schrödner, R., Bräuer, P., Wolke, R., and Herrmann, H.: An advanced modeling study on the impacts and atmospheric implications of multiphase dimethyl sulfide chemistry, P. Natl. Acad. Sci. USA, 113, 11776–11781, https://doi.org/10.1073/pnas.1606320113, 2016.

Holzer, C., Franzke, Y. J., and Pausch, A.: Current density functional framework for spin–orbit coupling, J. Chem. Phys., 157, 204102, https://doi.org/10.1063/5.0122394, 2022.

Kuhn, M. and Weigend, F.: Two-component hybrid time-dependent density functional theory within the Tamm-Dancoff approximation, J. Chem. Phys., 142, 034116, https://doi.org/10.1063/1.4905829, 2015.

Kulmala, M., Kontkanen, J., Junninen, H., Lehtipalo, K., Manninen, H. E., Nieminen, T., Petäjä, T., Sipilä, M., Schobesberger, S., Rantala, P., Franchin, A., Jokinen, T., Järvinen, E., Äijälä, M., Kangasluoma, J., Hakala, J., Aalto, P. P., Paasonen, P., Mikkilä, J., Vanhanen, J., Aalto, J., Hakola, H., Makkonen, U., Ruuskanen, T., Mauldin, R. L., 3rd, Duplissy, J., Vehkamäki, H., Bäck, J., Kortelainen, A., Riipinen, I., Kurtén, T., Johnston, M. V., Smith, J. N., Ehn, M., Mentel, T. F., Lehtinen, K. E., Laaksonen, A., Kerminen, V. M., and Worsnop, D. R.: Direct observations of atmospheric aerosol nucleation, Science, 339, 943–946, https://doi.org/10.1126/science.1227385, 2013.

Lehtinen, K. E. J., Dal Maso, M., Kulmala, M., and Kerminen, V.-M.: Estimating nucleation rates from apparent particle formation rates and vice versa: Revised formulation of the Kerminen–Kulmala equation, J. Aerosol Sci., 38, 988–994, https://doi.org/10.1016/j.jaerosci.2007.06.009, 2007.

Lehtipalo, K., Rondo, L., Kontkanen, J., Schobesberger, S., Jokinen, T., Sarnela, N., Kürten, A., Ehrhart, S., Franchin, A., Nieminen, T., Riccobono, F., Sipilä, M., Yli-Juuti, T., Duplissy, J., Adamov, A., Ahlm, L., Almeida, J., Amorim, A., Bianchi, F., Breitenlechner, M., Dommen, J., Downard, A. J., Dunne, E. M., Flagan, R. C., Guida, R., Hakala, J., Hansel, A., Jud, W., Kangasluoma, J., Kerminen, V.-M., Keskinen, H., Kim, J., Kirkby, J., Kupc, A., Kupiainen-Määttä, O., Laaksonen, A., Lawler, M. J., Leiminger, M., Mathot, S., Olenius, T., Ortega, I. K., Onnela, A., Petäjä, T., Praplan, A., Rissanen, M. P., Ruuskanen, T., Santos, F. D., Schallhart, S., Schnitzhofer, R., Simon, M., Smith, J. N., Tröstl, J., Tsagkogeorgas, G., Tomé, A., Vaattovaara, P., Vehkamäki, H., Vrtala, A. E., Wagner, P. E., Williamson, C., Wimmer, D., Winkler, P. M., Virtanen, A., Donahue, N. M., Carslaw, K. S., Baltensperger, U., Riipinen, I., Curtius, J., Worsnop, D. R., and Kulmala, M.: The effect of acid–base clustering and ions on the growth of atmospheric nano-particles, Nat. Commun., 7, 11594, https://doi.org/10.1038/ncomms11594, 2016.

Li, J., Ning, A., Liu, L., and Zhang, X.: Atmospheric Bases-Enhanced Iodic Acid Nucleation: Altitude-Dependent Characteristics and Molecular Mechanisms, Environ. Sci. Technol., 58, 16962–16973, https://doi.org/10.1021/acs.est.4c06053, 2024.

Li, J., Ning, A., Liu, L., Deng, X., and Zhang, X.: Supporting data for the study of the IA-MSA-DMA system, Zenodo [data set], https://doi.org/10.5281/zenodo.18984315, 2026.

Li, Y., Shen, J., Zhao, B., Cai, R., Wang, S., Gao, Y., Shrivastava, M., Gao, D., Zheng, J., Kulmala, M., and Jiang, J.: A dynamic parameterization of sulfuric acid–dimethylamine nucleation and its application in three-dimensional modeling, Atmos. Chem. Phys., 23, 8789–8804, https://doi.org/10.5194/acp-23-8789-2023, 2023.

Liakos, D. G., Guo, Y., and Neese, F.: Comprehensive Benchmark Results for the Domain Based Local Pair Natural Or-

bital Coupled Cluster Method (DLPNO-CCSD(T)) for Closed- and Open-Shell Systems, J. Phys. Chem. A., 124, 90–100, https://doi.org/10.1021/acs.jpca.9b05734, 2020.

Liu, L., Li, S., Zu, H., and Zhang, X.: Unexpectedly significant stabilizing mechanism of iodous acid on iodic acid nucleation under different atmospheric conditions, Sci. Total Environ., 859, 159832, https://doi.org/10.1016/j.scitotenv.2022.159832, 2023.

Liu, Y., Xie, H.-B., Ma, F., Chen, J., and Elm, J.: Amine-enhanced methanesulfonic acid-driven nucleation: Predictive model and cluster formation mechanism, Environ. Sci. Technol., 56, 7751–7760, https://doi.org/10.1021/acs.est.2c01639, 2022.

Lu, T. and Chen, F.: Multiwfn: a multifunctional wavefunction analyzer, J. Comput. Chem., 33, 580–592, https://doi.org/10.1002/jcc.22885, 2012.

Lu, T. and Chen, Q.: Shermo: A general code for calculating molecular thermochemistry properties, Comput. Theor. Chem., 1200, 113249, https://doi.org/10.1016/j.comptc.2021.113249, 2021.

Ma, F., Xie, H. B., Zhang, R., Su, L., Jiang, Q., Tang, W., Chen, J., Engsvang, M., Elm, J., and He, X. C.: Enhancement of atmospheric nucleation precursors on iodic acid-induced nucleation: Predictive model and mechanism, Environ. Sci. Technol., 57, 6944–6954, https://doi.org/10.1021/acs.est.3c01034, 2023.

McGrath, M. J., Olenius, T., Ortega, I. K., Loukonen, V., Paasonen, P., Kurtén, T., Kulmala, M., and Vehkamäki, H.: Atmospheric Cluster Dynamics Code: a flexible method for solution of the birth-death equations, Atmos. Chem. Phys., 12, 2345–2355, https://doi.org/10.5194/acp-12-2345-2012, 2012.

Mohd Zaki, N. H., Ali, A. M. M., Mohamad Taib, M. F., Wan Ismail, W. I. N., Sepeai, S., and Ramli, A.: Dispersion-correction density functional theory (DFT+D) and spin-orbit coupling (SOC) method into the structural, electronic, optical and mechanical properties of $CH_3NH_3PbI_3$, Comput. Condens. Matte., 34, e00777, https://doi.org/10.1016/j.cocom.2022.e00777, 2023.

Myllys, N., Kubečka, J., Besel, V., Alfaouri, D., Olenius, T., Smith, J. N., and Passananti, M.: Role of base strength, cluster structure and charge in sulfuric-acid-driven particle formation, Atmos. Chem. Phys., 19, 9753–9768, https://doi.org/10.5194/acp-19-9753-2019, 2019.

Neese, F.: The ORCA program system, WIREs Comput. Mol. Sci., 2, 73–78, https://doi.org/10.1002/wcms.81, 2012.

Ning, A. and Zhang, X.: The synergistic effects of methanesulfonic acid (MSA) and methanesulfinic acid (MSIA) on marine new particle formation, Atmos. Environ., 269, 118826, https://doi.org/10.1016/j.atmosenv.2021.118826, 2022.

Ning, A., Liu, L., Ji, L., and Zhang, X.: Molecular-level nucleation mechanism of iodic acid and methanesulfonic acid, Atmos. Chem. Phys., 22, 6103–6114, https://doi.org/10.5194/acp-22-6103-2022, 2022a.

Ning, A., Liu, L., Zhang, S., Yu, F., Du, L., Ge, M., and Zhang, X.: The critical role of dimethylamine in the rapid formation of iodic acid particles in marine areas, npj Clim. Atmos. Sci., 5, 92, https://doi.org/10.1038/s41612-022-00316-9, 2022b.

Ning, A., Shen, J., Zhao, B., Wang, S., Cai, R., Jiang, J., Yan, C., Fu, X., Zhang, Y., Li, J., Ouyang, D., Sun, Y., Saiz-Lopez, A., Francisco, J. S., and Zhang, X.: Overlooked significance of iodic acid in new particle formation in the continental atmosphere, P. Natl. Acad. Sci. USA, 121, e2404595121, https://doi.org/10.1073/pnas.2404595121, 2024.

O'Dowd, C. D. and de Leeuw, G.: Marine aerosol production: a review of the current knowledge, Philos. T. R. Soc. A., 365, 1753–1774, https://doi.org/10.1098/rsta.2007.2043, 2007.

Perraud, V., Horne, J. R., Martinez, A. S., Kalinowski, J., Meinardi, S., Dawson, M. L., Wingen, L. M., Dabdub, D., Blake, D. R., Gerber, R. B., and Finlayson-Pitts, B. J.: The future of airborne sulfur-containing particles in the absence of fossil fuel sulfur dioxide emissions, P. Natl. Acad. Sci. USA, 112, 13514–13519, https://doi.org/10.1073/pnas.1510743112, 2015.

Peterson, K. A., Figgen, D., Goll, E., Stoll, H., and Dolg, M.: Systematically convergent basis sets with relativistic pseudopotentials. II. Small-core pseudopotentials and correlation consistent basis sets for the post-d group 16–18 elements, J. Chem. Phys., 119, 11113–11123, https://doi.org/10.1063/1.1622924, 2003.

Quéléver, L. L. J., Dada, L., Asmi, E., Lampilahti, J., Chan, T., Ferrara, J. E., Copes, G. E., Pérez-Fogwill, G., Barreira, L., Aurela, M., Worsnop, D. R., Jokinen, T., and Sipilä, M.: Investigation of new particle formation mechanisms and aerosol processes at Marambio Station, Antarctic Peninsula, Atmos. Chem. Phys., 22, 8417–8437, https://doi.org/10.5194/acp-22-8417-2022, 2022.

Rong, H., Liu, J., Zhang, Y., Du, L., Zhang, X., and Li, Z.: Nucleation mechanisms of iodic acid in clean and polluted coastal regions, Chemosphere, 253, 126743, https://doi.org/10.1016/j.chemosphere.2020.126743, 2020.

Salignat, R., Rissanen, M., Iyer, S., Baray, J.-L., Tulet, P., Metzger, J.-M., Brioude, J., Sellegri, K., and Rose, C.: Measurement report: Insights into the chemical composition and origin of molecular clusters and potential precursor molecules present in the free troposphere over the southern Indian Ocean: observations from the Maïdo Observatory (2150 m a.s.l., Réunion), Atmos. Chem. Phys., 24, 3785–3812, https://doi.org/10.5194/acp-24-3785-2024, 2024.

Sarr, S., Graton, J., Rahali, S., Montavon, G. F., and Galland, N.: Delocalized relativistic effects, from the viewpoint of halogen bonding, Phys. Chem. Chem. Phys., 23, 4064–4074, https://doi.org/10.1039/D0CP05840H, 2021.

Scholz, W., Shen, J., Aliaga, D., Wu, C., Carbone, S., Moreno, I., Zha, Q., Huang, W., Heikkinen, L., Jaffrezo, J. L., Uzu, G., Partoll, E., Leiminger, M., Velarde, F., Laj, P., Ginot, P., Artaxo, P., Wiedensohler, A., Kulmala, M., Mohr, C., Andrade, M., Sinclair, V., Bianchi, F., and Hansel, A.: Measurement report: Long-range transport and the fate of dimethyl sulfide oxidation products in the free troposphere derived from observations at the high-altitude research station Chacaltaya (5240 m a.s.l.) in the Bolivian Andes, Atmos. Chem. Phys., 23, 895–920, https://doi.org/10.5194/acp-23-895-2023, 2023.

Sipilä, M., Sarnela, N., Jokinen, T., Henschel, H., Junninen, H., Kontkanen, J., Richters, S., Kangasluoma, J., Franchin, A., peräkylä, O., Rissanen, M. P., Ehn, M., Vehkamäki, H., Kurten, T., Berndt, T., Petäjä, T., Worsnop, D., Ceburnis, D., Kerminen, V. M., Kulmala, M., and O'Dowd, C.: Molecular-scale evidence of aerosol particle formation via sequential addition of HIO_3, Nature, 537, 532–534, https://doi.org/10.1038/nature19314, 2016.

Stolzenburg, D., Simon, M., Ranjithkumar, A., Kürten, A., Lehtipalo, K., Gordon, H., Ehrhart, S., Finkenzeller, H., Pichelstorfer, L., Nieminen, T., He, X.-C., Brilke, S., Xiao, M., Amorim, A., Baalbaki, R., Baccarini, A., Beck, L., Bräkling, S., Caudillo Murillo, L., Chen, D., Chu, B., Dada, L., Dias, A., Dommen, J.,

Duplissy, J., El Haddad, I., Fischer, L., Gonzalez Carracedo, L., Heinritzi, M., Kim, C., Koenig, T. K., Kong, W., Lamkaddam, H., Lee, C. P., Leiminger, M., Li, Z., Makhmutov, V., Manninen, H. E., Marie, G., Marten, R., Müller, T., Nie, W., Partoll, E., Petäjä, T., Pfeifer, J., Philippov, M., Rissanen, M. P., Rörup, B., Schobesberger, S., Schuchmann, S., Shen, J., Sipilä, M., Steiner, G., Stozhkov, Y., Tauber, C., Tham, Y. J., Tomé, A., Vazquez-Pufleau, M., Wagner, A. C., Wang, M., Wang, Y., Weber, S. K., Wimmer, D., Wlasits, P. J., Wu, Y., Ye, Q., Zauner-Wieczorek, M., Baltensperger, U., Carslaw, K. S., Curtius, J., Donahue, N. M., Flagan, R. C., Hansel, A., Kulmala, M., Lelieveld, J., Volkamer, R., Kirkby, J., and Winkler, P. M.: Enhanced growth rate of atmospheric particles from sulfuric acid, Atmos. Chem. Phys., 20, 7359–7372, https://doi.org/10.5194/acp-20-7359-2020, 2020.

Takashima, H., Kanaya, Y., Kato, S., Friedrich, M. M., Van Roozendael, M., Taketani, F., Miyakawa, T., Komazaki, Y., Cuevas, C. A., Saiz-Lopez, A., and Sekiya, T.: Full latitudinal marine atmospheric measurements of iodine monoxide, Atmos. Chem. Phys., 22, 4005–4018, https://doi.org/10.5194/acp-22-4005-2022, 2022.

Verstraete, M. J., Torrent, M., Jollet, F., Zérah, G., and Gonze, X.: Density functional perturbation theory with spin-orbit coupling: Phonon band structure of lead, Phys. Rev. B., 78, 045119, https://doi.org/10.1103/PhysRevB.78.045119, 2008.

Xia, D., Chen, J., Yu, H., Xie, H. B., Wang, Y., Wang, Z., Xu, T., and Allen, D. T.: Formation Mechanisms of Iodine-Ammonia Clusters in Polluted Coastal Areas Unveiled by Thermodynamics and Kinetic Simulations, Environ. Sci. Technol., 54, 9235–9242, https://doi.org/10.1021/acs.est.9b07476, 2020.

Yan, J., Jung, J., Zhang, M., Xu, S., Lin, Q., Zhao, S., and Chen, L.: Significant Underestimation of Gaseous Methanesulfonic Acid (MSA) over Southern Ocean, Environ. Sci. Technol., 53, 13064–13070, https://doi.org/10.1021/acs.est.9b05362, 2019.

Yu, F. and Luo, G.: Modeling of gaseous methylamines in the global atmosphere: impacts of oxidation and aerosol uptake, Atmos. Chem. Phys., 14, 12455–12464, https://doi.org/10.5194/acp-14-12455-2014, 2014.

Zhang, R., Khalizov, A., Wang, L., Hu, M., and Xu, W.: Nucleation and growth of nanoparticles in the atmosphere, Chem. Rev., 112, 1957–2011, https://doi.org/10.1021/cr2001756, 2012.

Zhang, R., Xie, H. B., Ma, F., Chen, J., Iyer, S., Simon, M., Heinritzi, M., Shen, J., Tham, Y. J., Kurtén, T., Worsnop, D. R., Kirkby, J., Curtius, J., Sipilä, M., Kulmala, M., and He, X. C.: Critical Role of Iodous Acid in Neutral Iodine Oxoacid Nucleation, Environ. Sci. Technol., 56, 14166–14177, https://doi.org/10.1021/acs.est.2c04328, 2022.